

Photon emission in scanning tunneling microscopy: Interpretation of photon maps of metallic systems

Richard Berndt* and James K. Gimzewski

IBM Research Division, Zurich Research Laboratory, CH-8803 Rüschlikon, Switzerland

(Received 16 April 1993)

We analyze maps of the integral photon intensity emitted from the tunneling gap of a scanning tunneling microscope obtained simultaneously with topography from a variety of metal films and single-crystal surfaces in ultrahigh vacuum. The effects of adsorbates and structures created with the scanning tunneling microscope on their local photon emission properties are investigated to explore the potential of the technique for chemical mapping. It is proposed that contrasts in photon maps on a scale of some tens of nanometers are attributable to local variations in the field strength of tip-induced plasmon modes which are determined by the surface geometry of the junction and its dielectric properties. On a (sub)nanometer scale, a second contrast mechanism is observed to occur, consistent with geometry-induced variations in the matrix element for inelastic tunneling. A comparison of electron spectroscopic data with bias-dependent photon maps indicates that contrasts on a subnanometer scale are further mediated by local modifications of the density of final states positioned one quantum of energy ($h\nu$) below the bottom of the elastic tunneling channel with respect to the Fermi level. These three mechanisms provide a framework for the interpretation of photon maps obtained on metallic systems.

I. INTRODUCTION

Use of a scanning tunneling microscope (STM) to study surface geometry and electronic structures locally¹ is based primarily on the tunneling current and its variation with experimental parameters. The dominant portion of this current arises from elastic tunneling. Studies of inelastic electron tunneling (IET) processes using the tunneling current in a STM are hampered by noise in the measured tunnel current. Following earlier proposals,^{2,3} we have demonstrated that IET excitation of tip-induced plasmon modes on metal surfaces can be monitored conveniently by studying photons emitted from the tunnel gap.⁴ In particular, detecting photons emitted from a STM allows access to a purely inelastic component of the tunnel current with a high signal-to-noise ratio. In a more general sense the electromagnetic interaction of two metallic objects in nanometer proximity may be probed using photon emission induced by tunneling. This approach should permit elucidation of the collective properties of nanostructured materials, clusters,⁵ and the role of electromagnetic coupling in surface-enhanced Raman scattering.⁶ In this paper we discuss simultaneous measurements of integral photon intensity (photon maps) and STM topographs of metals, and explore the geometric and electronic contributions that determine photon emission induced by tunneling electrons.

Photon emission from a STM has recently attracted the interest of a number of groups, and we shall subsequently review their work briefly.

The first results for semiconductors were reported for Si(111) surfaces where an emission of ultraviolet photons was detected.² The results showed similarities to conventional inverse photoemission⁷ and additional features that were assigned to optical transitions into field-

induced states. A more useful technique was local cathodoluminescence (CL), where emission from optical transitions between the band edges was detected. Abraham *et al.*⁸ used the tip of the STM to excite CL in GaAs/Ga_{1-x}Al_xAs heterostructures and have obtained photon maps of the quantum wells. Recent extensions of this work have enabled local band offset profiling of the structures.⁹ The mechanism involved here occurs underneath the surface due to recombination of injected electrons with holes in the GaAs. Luminescence for gold-passivated GaAs surfaces has been reported by Wenderoth, Gregor, and Ulbrich.¹⁰ For CdS(1120) surfaces, CL was spectrally resolved for injecting either electrons or holes from the tip into the semiconductor.¹¹ The optical spectra revealed both band-edge emission and deep trap states. More recently, polarization effects have been addressed using GaAs samples.¹² Ushioda has reported light emission spectra from Si(111) surfaces as well as measurements of the polarization.¹³ The first attempts at low-temperature STM studies of luminescence from InP have been made by Montelius, Pistol, and Samuelson.¹⁴ Interpretations of CL rely partly on what is known from conventional CL studies. However, many new and useful aspects of the method exist, particularly regarding the investigation of quantum-size effects, the mapping of CL from porous Si being a recent case.¹⁵

Photon emission from metal surfaces has also received much interest because the mechanism involved in the emission process is new and specific to the nanometer proximity and electromagnetic coupling of the tip to the surface. Understanding the underlying physics, however, is more complex and requires new approaches both from the theoretical and the experimental sides. Experiments are related to previous investigations of light emission from metal-oxide-metal (*M-O-M*) solid-state tunnel junc-

tions which was first discovered by Lambe and McCarthy in 1976.¹⁶ Many controversies still exist regarding the mechanisms involved in those experiments. With the STM, the freedom to vary experimental parameters on well-characterized surfaces has permitted detailed investigations of the processes involved, and several theoretical models have been invoked to describe the emission spectra.

The first observations of photon emission using the STM as a local excitation source^{2,3,17} were reported in 1988. It was demonstrated that a variety of modes of operation including isochromat spectroscopy, optical emission spectroscopy, and photon mapping can be used simultaneously with topography. For Ag polycrystalline surfaces, we proposed that IET (Ref. 17) was responsible for the excitation of localized plasmon modes at the surface, and presented a theoretical framework in Ref. 18 to establish the role of IET versus hot-electron injection as the excitation mechanism for localized plasmon modes based on the theory of Persson and Baratoff.¹⁹ Here, as in all subsequent theories, IET was found to dominate. The model of photon spectra emitted from a W-Ag tunnel junction set up by Johansson, Monreal, and Apell²⁰ showed qualitative similarities to published results.^{17,18} Recently, we have demonstrated that photon spectra can be modeled fairly well for Cu, Au, and (to a lesser extent) Ag surfaces.^{4,21} Uehara *et al.*²² recently also developed a theory for visible light emission from a STM by adapting a theory designed for a solid-state tunnel junctions. Their theory concerns the differences between the branching ratios of surface-plasmon polaritons that propagate along the surface and those localized under the tip [referred to here as tip-induced plasmon (TIP) modes], which emit directly. There are also a number of calculations dealing with near-field optics which relate to the electromagnetic properties of the tip-surface system, but to which we do not refer in detail since they do not include coupling of the tunnel electrons.^{23,24}

On the experimental side, with a few exceptions, the interpretation of the results of photon mapping is a formidable task. For experiments conducted in air, there are problems with contamination and electrical breakdown at the voltages used (2–5 V) (similar to *M-O-M* junctions). However, several reports on a variety of noble-metal surfaces have shown that photon mapping and spectroscopy are possible.^{25–30} Ushioda, Uehara, and Kuwahara³¹ have investigated the optical spectroscopy of Au surfaces under UHV conditions and found spectral features that agree with our data,⁴ although they did not identify the origin of these features. Experiments have been performed on thin Ag films deposited onto Si(111)-(7×7) surfaces, for which quite remarkable structures were found in the photon maps in the form of bands of high intensity.¹⁵ These bands show no correlation with topography and suggest an interference effect.

While it has been established that photon maps provide a new channel of information on the properties of a surface, a detailed framework for their interpretation has yet to be established. In this paper we present our current model for the analysis of photon maps based on simultaneous topographic, bias-dependent imaging and on a

variety of spectroscopic data from which the various factors that determine the local efficiency of photon emission can be disentangled. While the basic factors have been identified and described, there nevertheless exists a number of effects that require further evaluation, in particular for complex systems such as amorphous or polycrystalline materials. We shall concentrate here on well-defined surfaces, adsorption systems, and local modifications introduced by the STM tip. These samples represent as idealized a set of systems as possible, which are more directly amenable to the theoretical models developed to date. They are representative of our experimental approach in the stepwise fabrication of nanometer-scale light-emitting structures and of the broader goal of developing techniques to obtain local chemical information using a STM.

The outline of the paper is as follows: Sec. II reviews the current understanding of photon emission based on experimental spectroscopic results and theoretical model calculations to provide a foundation for the analysis of photon maps. Important experimental issues are addressed in Sec. III. Section IV covers the origins of contrasts in photon maps associated with topographic structures with typical dimensions of ~ 10 nm. Lastly, observations of contrast on a nanometer and subnanometer level are analyzed in Sec. V, and several specific contrast mechanisms are presented as well as methods to identify their contribution. The mechanisms proposed provide a general method for the interpretation of photon mapping in metallic systems and give an insight into the physical origin of factors governing inelastic tunneling excitation of photons in mesoscopic systems.

II. INELASTIC TUNNELING EXCITATION OF TIP-INDUCED PLASMON MODES

Our interpretation of photon maps is developed using both optical spectroscopic data^{4,32} and model calculations.^{19,20} While fluorescence spectra indicate that transition radiation and emission from surface plasmons occur on noble-metal surfaces in a STM at elevated tip voltages ($|V_t| \gtrsim 100$ V),⁴ an interesting phenomenon is observed in the tunneling regime ($|V_t| \lesssim 5$ V) and in the proximity field-emission regime ($|V_t| \lesssim 40$ V). In the latter, optical emission is redshifted with an enhanced quantum efficiency of $\sim 10^{-4}$ photons/electron for W tips on Ag. Similar results were observed on other noble-metal surfaces.⁴ Using STM, photon emission has also been detected from transition-metal surfaces on silicon,³³ and more recently from Pb islands on silicon.³⁴

Intensive photon emission has been interpreted as arising from the radiative decay of dipolar plasmons created and localized by the close proximity of a tip to a sample. A strong enhancement of the electromagnetic field of these modes below the tip apex is predicted,³⁵ and tunneling electrons which have a wave vector parallel to the dipole mode can couple efficiently via IET for solid-state tunneling junctions.¹⁶ It has also been proposed for (*M-O-M*) junctions that photon emission occurs via hot-electron injection.³⁶ However, in the STM experiments

discussed here the following observations suggest hot-electron excitation to be of negligible importance with respect to IET. First, the high intensities and lack of significant bias dependence observed are typical of a resonant process. Second, model calculations^{4,19,20,37} in which IET dominates show good agreement with experimental fluorescence spectra photon intensities for transition-metal tips. Furthermore, the observation of higher intensities and new spectral features found by using noble-metal tips,³⁸ as well as the angular distribution of the photon intensity,³² which is consistent with a dipolar antenna, are both in qualitative agreement with the IET-TIP mechanism. Also, using higher tip voltages, shifted field-emission resonances are detected in isochromat spectra, which we have previously discussed and found consistent with IET as opposed to hot-electron excitation of photons.⁴

The IET-TIP model implies that a variety of factors can affect the photon intensity on a local scale. Since the electromagnetic properties of the tip-sample region are determined by a field-enhancement term which in turn modifies the probability of IET, the tip-sample distance, characteristic tip radius, and sample curvature determine the local TIP modes. The lateral extent of these TIP modes on flat surfaces is theoretically determined to be of the order of ~ 10 nm,³⁷ and hence we can expect contrast in photon maps for surface features with geometric dimensions on that scale. On the other hand, electronic properties determine the initial and final density of states available for inelastic processes, and they will modify the branching ratio between elastic and inelastic channels and hence photon emission. The probabilities that nonradiative processes which compete with photon emission (such as electron-hole pair generation) will occur also vary on another characteristic scale with respect to radiative decay. Consequently, one expects local variations of such factors to give rise to contrast in maps of the integral photon intensity (photon maps). These are the basic concepts that we shall invoke to interpret photon maps and that can be tested by analyzing the geometric influence via topography and the electronic aspects via bias-dependent topography and spectroscopy.

III. EXPERIMENT

The experimental configuration used has been described in detail elsewhere.³⁹ Briefly, our purpose-built STM operates in UHV and is surrounded by an ellipsoidal mirror to focus light from the tip region, which lies in the principal focus of the reflector, on the second focal point outside the vacuum chamber close to a sapphire viewport. Photomultipliers or a grating spectrometer and intensified diode array detector are used to detect and spectrally resolve the emission. Cu(111), Ag(111), and Au(110) surfaces were prepared by repeated cycles of Ne-ion bombardment and subsequent annealing. X-ray photoemission spectroscopy (XPS) and low-energy electron diffraction were used to monitor surface contamination and ordering. We used etched W tips heated in UHV to 1000 °C and then sharpened by Ne-ion bombardment. Ti films (thickness exceeding 2000 Å) were evaporated in

UHV onto Si(111) surfaces. Using XPS, a submonolayer contamination (coverage < 0.1 monolayer) by carbon and oxygen was found. Oxygen adsorption was studied by exposing freshly evaporated Ti films to molecular oxygen (pressure 10^{-7} torr) at room temperature. The adsorption was monitored using XPS of the Ti $2p^{3/2}$, O $1s$, and C $1s$ regions.

IV. LONG-RANGE CONTRAST

Topographs obtained on thick silver films condensed onto Si(111) display preferred (111) texture with grain sizes in the 200–500-Å range.¹⁸ The corresponding photon maps contain clearly contrasting regions relating to individual grains. Some grains give rise to strong emission (exceeding 10 kcps/nA), while no emission was detected from other grains. Recently, several other groups have also investigated optical emission from similarly structured polycrystalline films using a STM.^{25–29} The interpretation of these images is complicated by the structural complexity of the metallic films and in particular by the columnar extension of the grains beneath the surface which determines coupling between grains. In addition, adjacent grains may modify both the field distribution and relative probabilities of various decay mechanisms.¹⁸ Owing to surface roughness on a scale of a few hundred Å, the tip is also likely to interact electromagnetically with several grains simultaneously, resulting in a variety of local modes. Moreover, adsorbate layers can effectively diminish the detected photon intensity and will be discussed below. Preferential adsorption of residual gases contributes to intensity variations, in particular to distinct intrainland intensity variations observed in certain samples. Nevertheless, these images give a feeling for the richness of factors that determine photon maps and differentiate them from topographs.

Clearly, a deeper understanding of the factors that give rise to photon emission requires experiments on more well-defined surfaces.

In order to control the shape of the surface, one can take advantage of the capability of the STM to modify surface structures locally⁴⁰ to study model systems such as small single particles on otherwise flat single-crystal surfaces. An example of this approach for a Cu(111) surface modified prior to measurement by applying short negative voltage pulses to the tip is shown in Fig. 1(a). Such pulses were in some but not all cases found to result in the formation of protrusions. In the example shown, a protruding structure with apparent dimensions of 50 Å in height and some 250 Å in diameter was generated [see cross section in Fig. 1(c) for details]. Additionally, a dislocation network appearing as lines crossing at angles of $\sim 60^\circ$ was also observed. It is important to note here that the real shape of a protrusion may differ from the STM topograph since the roughness of the protrusion and tunnel tip may be comparable, giving rise to a contribution to the topography corresponding to the tip shape, and thereby changing the tunneling filament on the tip. The photon map observed simultaneously with topography and a cross section thereof are displayed in Figs. 1(b) and 1(d), respectively. While the detected photon intensi-

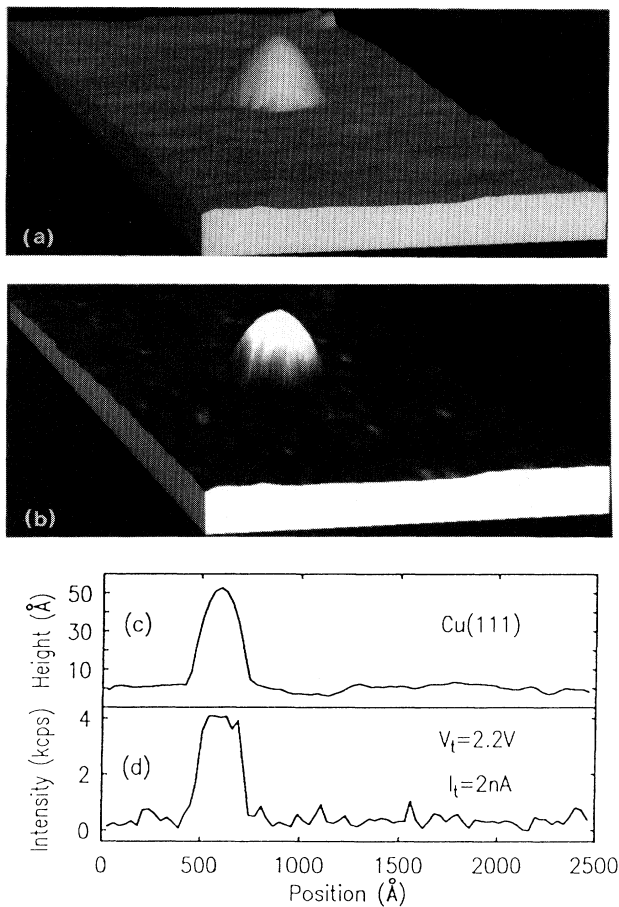


FIG. 1. $1600 \times 2000\text{-}\text{\AA}^2$ subarea of a topograph of a Cu(111) surface ($V_t = 2.2$ V and $I_t = 2$ nA) (a) Topograph (height scale: 50 \AA) rendered as a pseudo-three-dimensional object. (b) Image (a) with photon intensity data superimposed as a grey scale coloration corresponding to 0 – 2000 cps. (c) and (d) Cross sections of original topograph and photon map, respectively.

ty is fairly uniform above flat Cu(111) regions, a pronounced increase in emission by approximately one order of magnitude is found when the tip is scanned over the protrusion. This local increase in intensity is in accordance with theoretical predictions of the intensity as a function of particle size, which predict an increase in photon emission from small structures relative to a flat surface.¹⁹ Furthermore, the sharp contrast occurring in the photon map demonstrates that the emission is due to a localized mode between the tip and the protrusion as opposed to the roughness-mediated decay of a propagating surface plasmon. If the latter were applicable, then the protrusion would act as a scattering center facilitating the conversion of plasmons into photons. In that case a slow decay of intensity with increasing distance from the structure over the mean plasmon decay length [> 1 μm (Ref. 41)] would be expected. Kroo *et al.* have demonstrated such a slow decay over > 1 μm , using a STM to detect propagating plasmon waves launched by photons in a Kretschman configuration.⁴² The increase

in intensity at the protrusion is also consistent with a copper-containing protrusion. Other materials present in the surface region, such as residual gases, tungsten from the tip, or tip contaminants that might have formed the structure when the voltage pulse was applied, would drastically reduce the emission intensity with respect to a flat clean copper surface, and will be elaborated on below. The observations suggest that photon maps provide information on the chemical nature of a surface structure.⁴³ Further examples of the chemical mapping potential of photon emission are presented below.

Results similar to those for Cu structures were also obtained for silver crystallites. Such crystallites are prepared by condensing a thin Ag film (300 \AA) onto Si(111) followed by annealing to 490 K. The topograph and accompanying photon map of an isolated oblate-spherical silver grain (roughly 200 \AA in diameter and 50 \AA in height) against a relatively flat background are shown in Fig. 2. In accordance with the above discussion, the crystallite generates considerably higher photon signals than the flat surface areas do.

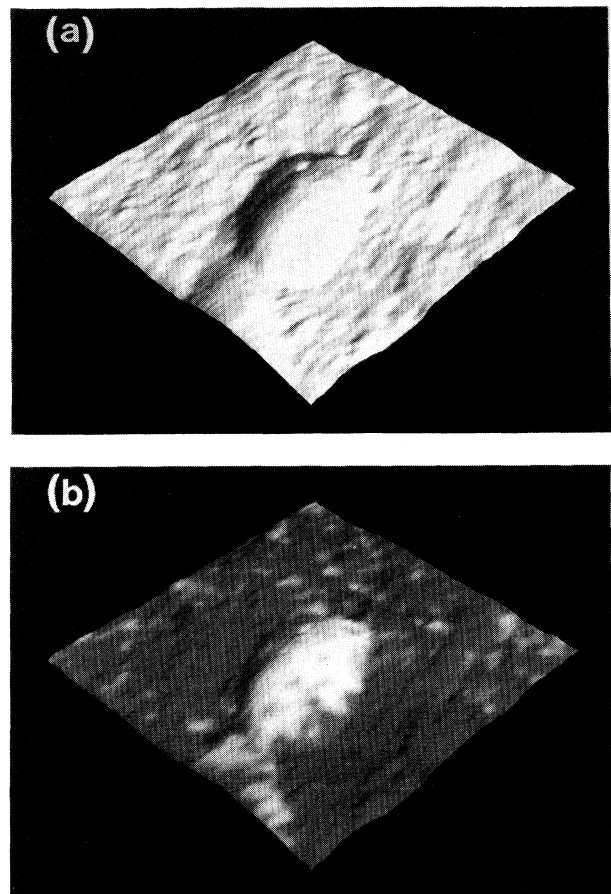


FIG. 2. Topography (edge enhanced) (a) and photon intensity map (b) of a $\sim 300\text{-}\text{\AA}$ -thick Ag film on Si(111) annealed at 490 K. Scan area: 350×350 \AA^2 , $V_t = -3.4$ V, $I_t = 1.5$ nA; height scale: 50 \AA ; photon intensity scale: 3000 cps.

V. SHORT-RANGE CONTRAST

The changes in the probability of excitation and decay via radiation give rise to the long-range contrast discussed in Sec. IV in terms of the radii of the particles supporting the plasmon mode. In addition, even finer details may be spatially resolved in photon maps which are incompatible with such a contrast mechanism. In particular, topographic variations on an atomic scale can also significantly change the probability for photon emission.

The STM topograph shown in Fig. 3(a) was acquired on a Cu(111) single crystal and consists of atomically flat surface areas separated by monatomic to triple-atomic steps. The line of protrusions running horizontally through the image was engineered by a controlled sequence of tip-surface contacts. The resulting nanostructures have an apparent lateral extent of approximately 20 Å in diameter and 2 Å in height and are most likely due to foreign material transferred by this procedure from the tip to the surface. The corresponding photon map [Fig. 3(b)], acquired simultaneously with topography illustrates that flat areas appear as relatively homogeneous sources of photon emission, cf. Fig. 1. One observes on the protrusions that photon emission is reduced by more than one order of magnitude. We can rule out that the variation in photon intensity arises from variations in I_t by determining that no direct correlation in structure is observable in simultaneously recorded maps of the tunnel-

ing current. Instead, the contrast in photon mapping observed at steps and protrusions, which occurs on the atomic scale, may be interpreted in terms of the excitation process of the TIP modes. Variations of the branching ratio of the inelastic current channel with respect to the elastic as well as other nonradiative channels will result in variations on a lateral scale comparable to the resolution of the STM working in the topographic mode. Hence, the ratio of the inelastic portion is expected to be sensitive to atomic configurations such as steps or adsorbate structures over lateral dimensions defined by the excitation volume of the tunneling electrons. The variations in photon intensity observed in Figs. 3(a) and 3(b) are consistent with this interpretation.

Given that the tunneling probability depends exponentially on the momentum of an electron in the direction vertical to a metal surface, the tunneling current density is typically peaked along the surface normal.⁴⁴ When the tip is in close proximity to a defect, the average tunneling current vector can cease to be parallel to the dipole moment of the TIP mode, whereas the dipole moment of the TIP mode itself, which gives rise to photon emission, stays almost unchanged due to its relatively large lateral extent. The vector mismatch reduces the matrix element for inelastic transitions which contains the square of the inner product of the current and dipole moments.³⁷ If one assumes in a simplistic model that the current is approximately perpendicular to the surface, and that the orientation of the dipole moment is constant, then the inelastic tunneling probability is proportional to $\cos^2(\alpha)$, where α is the angle between the surface normal and the tip axis. This quantity is plotted in Fig. 4(a) for the double-atomic step *S* shown in Fig. 3. The curve exhibits a close similarity to the experimental data in Fig. 4(b), lending support to the mechanism outlined above. On this basis, one expects that local geometric effects play a decisive role in photon emission and that their contribu-

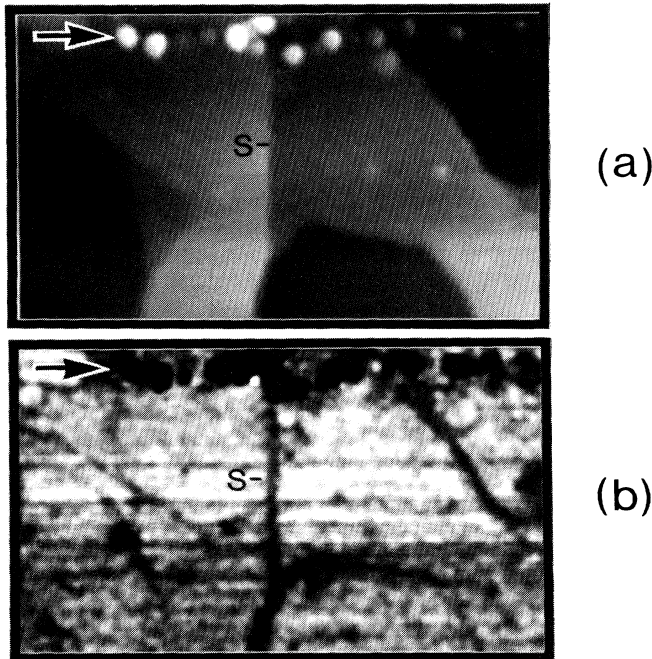


FIG. 3. (a) Constant current topography and (b) photon STM images of a Cu(111) surface exhibiting terraces separated by steps (see marker *S*, for instance) and small structures indicated by arrows which were created by a series of electric-field pulses at positive tip polarity. $V_t = 2.2$ V, $I_t = 5$ nA. Area = 500×300 Å²; intensity scale = 6000 cps. From Ref. 4.

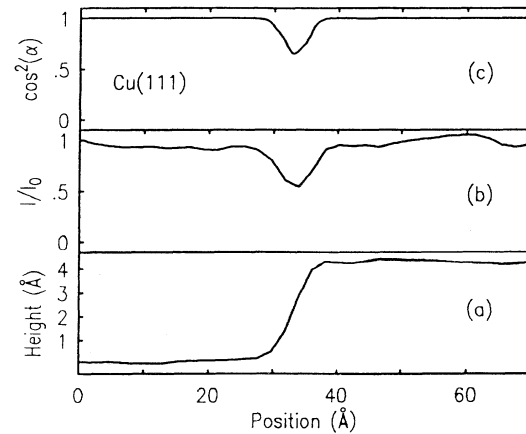


FIG. 4. Cross sections through step (*S*) marked in Fig. 3 from (a) the topograph and (b) the photon map. The intensity I has been normalized by division by the average intensity $I_0 = 5$ cps. (c) $\cos^2(\alpha)$, α being the angle between the surface normal and the tip axis (see text).

tion can be evaluated from the topographic structure observed in the accompanying topograph.

The contrasts observed at protrusions are not explainable by local geometric effects alone. An additional mechanism contributes to the intensity reduction observed at protrusions (see arrows in Fig. 3). Adsorbed material that appears as a protrusion increases the distance between tip and underlying *metal* substrate. This in turn reduces the field enhancement of the tip-induced modes, which depends on distance and, hence, on the probability of inelastic tunneling. Both measurements of the distance dependence of photon yield³² and model calculations⁴⁵ show that the decrease of the field strength is too small to account for the intensity reductions (more than one order of magnitude) observed at protrusions measured to be only 2 Å high. We shall now evaluate the role of the local density of states in mediating local photon emission.

The effect of adsorbates on photon emission of Ti films³³ that have been exposed to oxygen provides a system for which the influence of electronic structure can be conveniently analyzed. Oxygen adsorption on titanium gives rise to the formation of topographic structures that are dependent on bias voltage. These structures appear as prominent protrusions when imaged at negative V_t (1–2 Å in height and 10–20 Å in lateral extent), whereas they appear as shallow depressions at positive V_t . Steps show similar characteristics. The density of the structures increases with increasing exposure to O_2 . This increase is also accompanied by an increase in the intensity ratio of the O 1s to the Ti $2p^{3/2}$ peak areas, from <0.03 to 0.35 in XPS recorded from the samples. From these observations we determine the majority of structures to be oxygen induced. A detailed interpretation of the topographs in terms of local modifications of the local density of states of the surface induced by oxygen is available elsewhere.³⁸ The STM probes unoccupied states at the sample surface eV_t above E_F at $V_t < 0$ V, and the density of these states is locally increased by O adsorption,⁴⁶ hence protrusions are observed in STM images at $V_t < 0$ V. In contrast, at $V_t > 0$ V, electrons from occupied states between E_F and $E_F - eV_t$ contribute to the tunneling current, which results in a decrease of the density of these states consistent with the observation of depressions in STM topographs. These observations are also in qualitative agreement with ultraviolet photoelectron spectroscopy (UPS) (Ref. 47) and inverse photoemission spectroscopy (IPES) (Ref. 46) results, which (in a laterally averaged measurement) show similar trends for occupied and unoccupied states, respectively, upon O_2 adsorption. The STM results go further than photoemission in demonstrating that steps preferentially react with O_2 .

It is notable that variations of photon intensity introduced by the oxygen-related structures on Ti are observed on a length scale similar to the topographic data. The photon map shown in Fig. 5(b) was recorded simultaneously with the topography shown in Fig. 5(a). Inspection of the images reveals that the emission intensity is significantly diminished at steps (S_1, S_2) and also at oxygen-related structures (see marker O for an example). The latter is illustrated in a more quantitative manner in

Figs. 5(c) and 5(d) by a cross section of a small surface area containing three protrusions (1–2 Å in height and 10–20 Å in lateral extent). Comparison with the corresponding photon signal [Fig. 5(d)] shows that emission is decreased by up to one order of magnitude at these structures, with the lateral extent of the intensity minima being identical to the dimensions of the protrusions in the STM image [Fig. 5(a)]. Similar to our observations for structures written with the STM tip on Cu(111) (Fig. 3), the intensity reduction at adsorbates is again larger than that expected for purely geometric effects discussed previously. To investigate this interesting phenomenon in

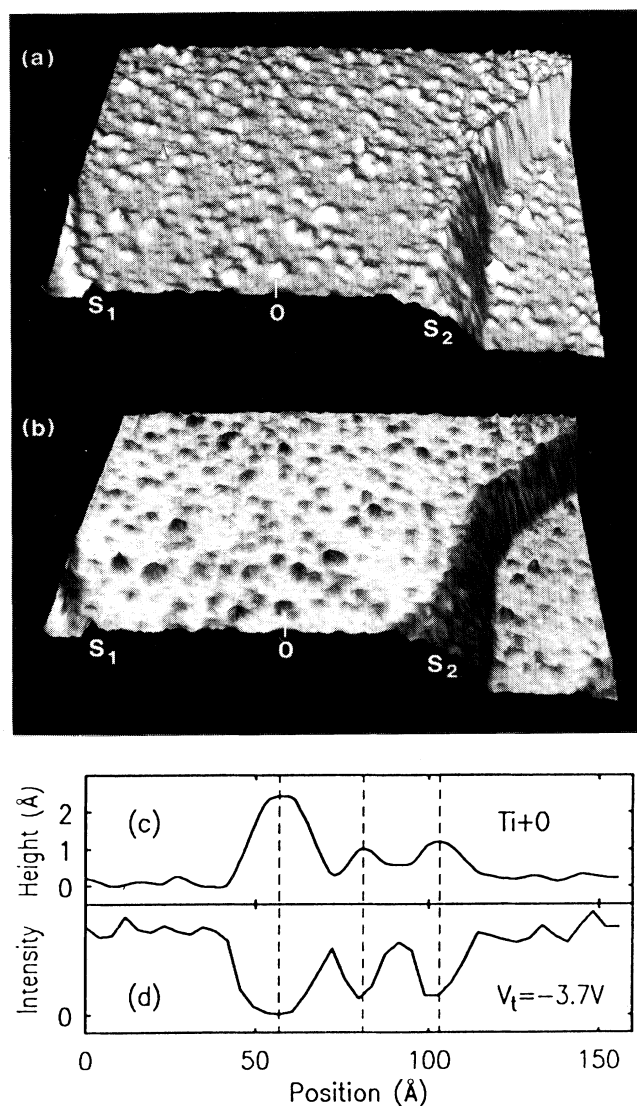


FIG. 5. (a) The STM topograph of a Ti film exposed to 20 L of O_2 at room temperature (area: $1000 \times 1000 \text{ \AA}^2$; height: 20 Å, $I_t = 50 \text{ nA}$, $V_t = -3.7 \text{ V}$). Examples of steps [S_1, S_2 and oxygen-induced structures (O)] are marked. (b) A photon map recorded simultaneously (intensity scale: 1000 cps). (c) and (d) Cross sections through an area containing three oxygen-related structures. Dashed lines serve to guide the eye. From Ref. 33.

more detail, the voltage dependence of constant-current topographs and photon maps was studied over a wide range of tip voltages. Figure 6 shows examples of topographs [Figs. 6(a) and 6(c)] and corresponding photon maps [Figs. 6(b) and 6(d)] measured at $V_t = -3.7$ and 3.6 V, respectively, on an area containing three terraces separated by steps of monoatomic height. A comparison of the topographies in Figs. 6(a) and 6(c) reveals some lateral drift. The major features, however, are readily identified in both images. Oxygen-induced structures appear as protrusions at $V_t < 0$ V and are invisible within the noise level and resolution of this particular experimental run at $V_t > 0$ V.³⁸ Similarly, the appearance of the steps changes from covered in Fig. 6(a) to clean in Fig. 6(b). The topography [Fig. 6(a)] and photon maps [Fig. 6(b)] confirm our observation in Fig. 5 of a sharp photon intensity contrast occurring at adsorbate sites and steps at negative tip bias. For reversed bias the photon map [Fig. 6(d)] is distinctly different. Contrast at oxygen sites is not observed at the given signal-to-noise ratio and only a faint indication of contrast is observed near the steps. The signal-to-noise ratio can be improved by taking cross sections of the images in Fig. 6 using the following technique. A stripe (~ 110 Å long, ~ 30 Å wide) at right angles through a step was extracted and averaged along the short direction. The resulting data, shown in Fig. 7, for $V_t = -3.7$ V demonstrate that the photon intensity [Fig. 7(b)] is reduced when the tip is located above the oxygen hillock situated at a step [Fig. 7(a)] by approximately one order of magnitude, whereas with reversed bias conditions [Fig. 7(d)] only a slight decrease in intensity is observed.

This phenomenon is visualized in Fig. 8, where contour lines corresponding to reduced photon intensity in the photon maps in Fig. 6 have been superimposed on the to-

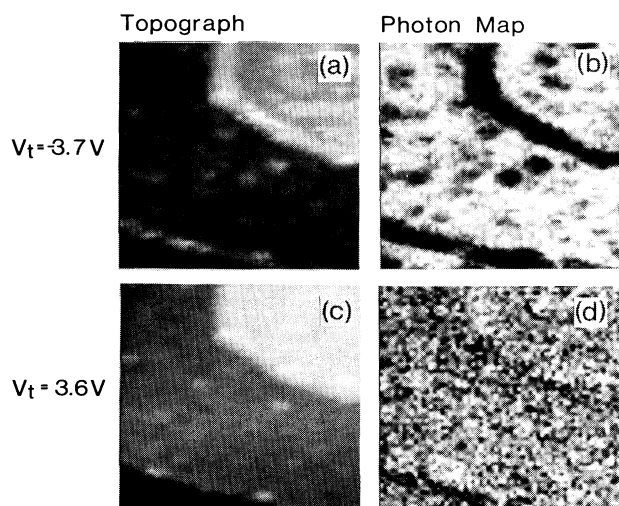


FIG. 6. Bias dependence of STM topographs (a) and (c) and photon maps (b) and (d) of a Ti film exposed to 20 L of molecular oxygen. $I_t = 10$ nA, $V_t = -3.7$ (top row) and 3.6 V (bottom row); area: 170×170 Å²; height scale: 7 Å; intensity scale: 0–200 cps.

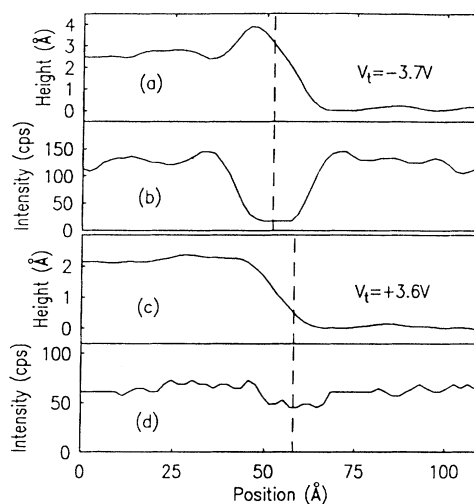


FIG. 7. Cross sections perpendicular to the step in the upper right corner of Fig. 6. It should be noted that cross sections (a)–(d) refer to exactly the same surface area. Between (a) and (c), however, no exact correlation is possible due to lateral drift. The lateral positions of the centers of the dark regions in photon maps are marked with dashed lines.

pographs. Each of the photon maps was averaged to improve the signal-to-noise ratio prior to the generation of the contour plot. At $V_t = -3.7$ V [Fig. 8(a)], less intensity is detected from adsorbate-induced protrusions on the terraces and at the steps than on the flat surface. However, at $V_t = 3.6$ V [Fig. 8(b)], the region of lower emission extends on the lower terrace in the vicinity of the step. The resulting offset between the step and the dark region is a further indication that the large intensity reduction is not caused exclusively by the geometric mechanism found previously at steps, but rather that the darker surface region contains adsorbates that are invisible in the topograph at the tunneling conditions used ($V_t > 0$ V) and that affect the photon emission. Consequently, geometric effects alone do not explain the order-of-magnitude reduction in intensity induced by adsorbates at $V_t < 0$ V on Ti.

Both tunneling current and photon intensity depend strongly on the density of states (DOS) of tip and sample. The effect of the DOS for elastic tunneling⁴⁸ is also ap-

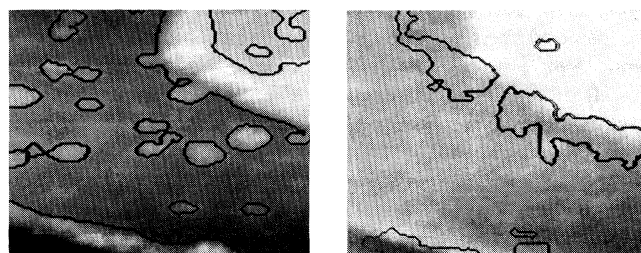


FIG. 8. Topographs of Fig. 6 with contour lines of the corresponding photon maps. Each of the photon maps was averaged before the contour plots were generated. (a) $V_t = -3.7$ V; contour level: 90 cps; and (b) $V_t = 3.6$ V, contour level: 55 cps.

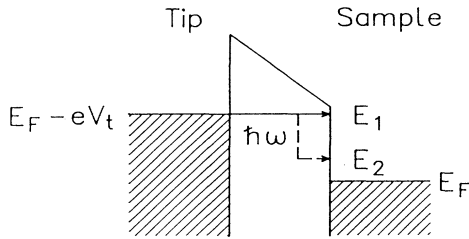


FIG. 9. A schematic energy diagram of a tunneling barrier for a negatively biased tip. Solid line: elastic tunneling; dashed line: inelastic tunneling. E_F stands for the Fermi energy of the sample, V_t for the tip voltage, $h\nu$ for the photon energy.

appropriate for IET and photon emission in that the density of final states, lying one photon quantum in energy ($h\nu$) below the elastic tunneling channel, controls the probability of IET.⁴ The direct consequences for the interpretation of photon maps are as follows. Recalling that at $V_t < 0$ V electrons tunnel from occupied levels of the tip to unoccupied states of the sample (cf. Fig. 9) owing to the sharp decay of tunneling probability with barrier height, occupied states close to the Fermi level of the tip contribute most efficiently to I_t . Consequently, the unoccupied DOS of the sample at $E_1 = E_F - eV_t$ determines the elastic tunneling channel. Inelastic processes probe a different window of empty sample states centered around $E_2 = E_1 - h\nu$. Given the constant current mode of operation of the STM (elastic channel), variations in the electronic structure at E_2 govern the probability of inelastic tunneling. Therefore, we propose that the high spatial resolution observed in these photon maps at oxygen-induced structures arises predominantly from modifications in the unoccupied DOS of the sample, resulting in the observed local variations of the branching ratio for elastic to inelastic tunneling. To test this, the photon emission data in Figs. 6–8 for $V_t < 0$ V are compared to electron-spectroscopic measurements of the unoccupied DOS of clean Ti and of Ti that has been exposed to O_2 .

IPES data^{46,49} for O absorbed on Ti show that O adsorption causes an increase in empty DOS at energies $E \gtrsim E_F + 2$ eV and a reduction for $E \lesssim E_F + 2$ eV.⁴⁶ In the STM experiment at $V_t = -3.7$ V, elastic tunneling probes the DOS at $E_1 = E_F + 3.7$ eV, which is increased at adsorbates, resulting in a protrusion.³⁸ For the photomultipliers used in the STM experiment,⁵⁰ the highest detection efficiency occurs for photons at $h\nu \sim 2.5$ eV. Consequently, the photon intensity arising from inelastic

tunneling is most sensitive to the DOS at $E_2 \sim E_F + 1.2$ eV, which is decreased on oxygen-covered Ti. This corresponds to a lower probability for inelastic tunneling and hence a reduced intensity, as observed in photon maps, thus confirming the above proposal.

At reversed bias ($V_t > 0$ V), tunneling occurs from filled sample states close to E_F to empty tip states at E_F and $E_F - h\nu$ for elastic and inelastic tunneling, respectively. The same sample DOS is probed by both tunneling channels, providing an adequate reason for the reduced contrast in photon maps at $V_t > 0$ V.

The mechanisms discussed above are likely to be present on the tip surface as well. The motion of tip atoms or adsorbates on the tip is probably responsible for sudden changes in intensity that give rise to horizontal, i.e., along the slow scan direction, stripes in the photon maps [see the middle of Fig. 3(b)]. These stripes are often closely correlated with sudden changes in apparent surface height by noninteger multiples of monoatomic step heights. In repeated scans of the same surface area, the frequency and positions of the stripes vary randomly. Both these observations are in accordance with the hypothesis of changes in tip structure during the scan. Similar results to those on Cu were obtained on atomically flat areas of Ag films.¹⁸

In summary, we have demonstrated that photon maps exhibit clear contrasts on different length scales. On the scale of ~ 10 nm, contrast reflects variations in the field strength of TIP modes governed by local surface geometry and dielectric function. On a subnanometer scale, contrast occurs due to geometry-induced changes of the matrix element for inelastic tunneling. Based on a comparison of the electron spectroscopic results with bias-dependent photon maps, however, we propose that a contrast on this scale is predominantly mediated by local modifications of the density of final states which lie one photon energy below the elastic tunneling channel. Spectroscopic and bias-dependent imagery of topographs and photon maps permit these contributions to be distinguished, and provide a framework for the interpretation of photon maps.

ACKNOWLEDGMENTS

We are grateful to Alexis Baratoff, Peter Johansson, Dieter Pohl, and Jürgen Sass for many clarifying discussions. We wish to thank Reto Schlittler for expert assistance in designing the photon STM and in preparing the crystals. H. Rohrer, B. Reihl, H. J. Güntherodt, and H. Saleminck are acknowledged for their support during this work.

*Present address: Université de Lausanne, Institut de Physique Expérimentale, CH-1015 Lausanne, Switzerland.

¹R. J. Behm, in *Scanning Tunneling Microscopy and Related Methods*, edited by R. J. Behm, N. Garcia, and H. Rohrer, Vol. 184 of *NATO Advanced Studies Institute Series E: Applied Sciences* (Kluwer, Dordrecht, 1990), p. 173; R. M. Feenstra, *ibid.*, p. 211.

²J. K. Gimzewski, B. Reihl, J. H. Coombs, and R. R. Schlittler, *Z. Phys. B* **72**, 497 (1988).

³J. H. Coombs, J. K. Gimzewski, B. Reihl, J. K. Sass, and R. R. Schlittler, *J. Microscopy* **152**, 325 (1988).

⁴R. Berndt, J. K. Gimzewski, and P. Johansson, *Phys. Rev. Lett.* **67**, 3796 (1991).

⁵R. Berndt, J. K. Gimzewski, and R. R. Schlittler, *Proceedings*

- of the 6th International Symposium on Small Particles and Inorganic Clusters "ISSPIC-6" [Z. Physik D (to be published)].
- ⁶A. Otto, I. Mrozek, H. Grabhorn, and W. Akemann, J. Phys. Condens. Matter **4**, 1143 (1992); M. Moskovits, Rev. Mod. Phys. **57**, 783 (1985).
- ⁷B. Reihl, Surf. Sci. **162**, 1 (1985).
- ⁸D. L. Abraham, A. Veider, Ch. Schönenberger, H. P. Meier, D. J. Arent, and S. F. Alvarado, Appl. Phys. Lett. **56**, 1564 (1990).
- ⁹P. Renaud and S. F. Alvarado, Phys. Rev. B **44**, 6340 (1991).
- ¹⁰M. Wenderoth, M. J. Gregor, and R. G. Ulbrich, Solid State Commun. **83**, 535 (1992).
- ¹¹R. Berndt and J. K. Gimzewski, Phys. Rev. B **45**, 14 095 (1991).
- ¹²S. F. Alvarado and P. Renaud, Phys. Rev. Lett. **68**, 1387 (1992).
- ¹³S. Ushioda, Solid State Commun. **84**, 173 (1992).
- ¹⁴L. Montelius, M.-E. Pistol, and L. Samuelson, Ultramicroscopy **42-44**, 210 (1992).
- ¹⁵J. K. Gimzewski, R. Berndt, R. R. Schlittler, A. W. McKinnon, M. E. Welland, T. M. H. Wong, Ph. Dumas, M. Gu, C. Syrykh, F. Salvan, and A. Hallimaoui, *NATO Advanced Research Workshop on Near Field Optics*, edited by D. W. Pohl and D. Courjon (Kluwer Academic, Dordrecht, in press).
- ¹⁶J. Lambe and S. L. McCarthy, Phys. Rev. Lett. **37**, 923 (1976).
- ¹⁷J. K. Gimzewski, J. K. Sass, R. R. Schlittler, and J. Schott, Europhys. Lett. **8**, 435 (1989).
- ¹⁸R. Berndt, A. Baratoff, and J. K. Gimzewski, in Ref. 1, pp. 269–280.
- ¹⁹B. N. J. Persson and A. Baratoff, Phys. Rev. Lett. **68**, 3224 (1992).
- ²⁰P. Johansson, R. Monreal, and P. Apell, Phys. Rev. B **42**, 9210 (1990).
- ²¹R. Berndt and J. K. Gimzewski, Surf. Sci. **269/270**, 556 (1992).
- ²²Y. Uehara, Y. Kimura, S. Ushioda, and K. Takeuchi, Jpn. J. Appl. Phys. **31**, 2465 (1992).
- ²³For a review of scanning near-field optical microscopy, see D. W. Pohl, in *Advances in Optical and Electron Microscopy* (Academic, London, 1991), Vol. 12, p. 243.
- ²⁴*Proceedings of NATO Advanced Research Workshop on Near Field Optics* (Ref. 15).
- ²⁵N. Venkateswaran, K. Sattler, J. Xhie, and M. Ge, Surf. Sci. **274**, 199 (1992).
- ²⁶V. Sivel, R. Coratger, F. Ajustron, and J. Beauvillain, Phys. Rev. B **45**, 8634 (1992).
- ²⁷I. I. Smolyaninov, V. S. Edelman, and V. V. Zavyalov, Phys. Lett. A **158**, 337 (1991).
- ²⁸I. I. Smolyaninov and E. V. Moskovets, Phys. Lett. A **165**, 252 (1992).
- ²⁹M. J. Gallagher, S. Howells, L. Yi, and D. Sarid, Surf. Sci. **278**, 270 (1992).
- ³⁰M. Bischoff, R. Elm, H. Pagnia, and C. Sprössler, Int. J. Electron. **73**, 1091 (1992).
- ³¹S. Ushioda, Y. Uehara, and M. Kuwahara, Appl. Surf. Sci. **60/61**, 448 (1992).
- ³²R. Berndt, Ph.D. thesis, University of Basel, Switzerland, 1992.
- ³³Further details on photon emission from transition metals are discussed in R. Berndt, J. K. Gimzewski, and R. R. Schlittler, Ultramicroscopy **42-44**, 355 (1992).
- ³⁴F. Salvan (private communication).
- ³⁵T. Takemori, M. Inoue, and K. Ohtaka, J. Phys. Soc. Jpn. **56**, 1587 (1987).
- ³⁶J. R. Kirtley, T. N. Theis, and J. C. Tsang, Appl. Phys. Lett. **37**, 435 (1980); Phys. Rev. B **24**, 5650 (1981); J. R. Kirtley, T. N. Theis, J. C. Tsang, and D. J. DiMaria, *ibid.* **27**, 4601 (1983).
- ³⁷P. Johansson, Ph.D. thesis, Physics Department, Chalmers University, Göteborg, Sweden, 1991.
- ³⁸R. Berndt, J. K. Gimzewski, and R. R. Schlittler (unpublished).
- ³⁹R. Berndt, R. R. Schlittler, and J. K. Gimzewski, J. Vac. Sci. Technol. B **9**, 573 (1991).
- ⁴⁰C. F. Quate, in *Proceedings of the NATO Science Forum '90, Highlights of the Eighties and Future Prospects in Condensed Matter Physics*, edited by L. Esaki (Plenum, New York, 1992).
- ⁴¹F. Abeles, in *Electromagnetic Surface Excitations*, edited by R. F. Wallis and G. I. Stegeman (Springer, Berlin, 1986).
- ⁴²N. Kroo, J.-P. Thost, M. Völcker, W. Krieger, and H. Walther, Europhys. Lett. **15**, 289 (1991).
- ⁴³J. K. Gimzewski and R. Berndt, *NATO Advanced Research Workshop on Manipulations of Atoms under High Fields and Temperatures: Applications*, edited by V. Thien Binh, N. Garcia, and K. Dransfeld (Kluwer, Dordrecht, 1993), Vol. 235, p. 219.
- ⁴⁴E. L. Wolf, *Principles of Electron Tunneling Spectroscopy* (Oxford University Press, New York, 1985), p. 23.
- ⁴⁵R. Berndt, J. K. Gimzewski, and P. Johansson (unpublished).
- ⁴⁶R. Konishi, S. Ikeda, T. Osaki, and H. Sasakura, Jpn. J. Appl. Phys. **29**, 1805 (1990).
- ⁴⁷E. Bertel, R. Stockbauer, and T. E. Madey, Surf. Sci. **141**, 355 (1984); B. M. Biwer and S. L. Bernasek, *ibid.* **167**, 207 (1986).
- ⁴⁸R. J. Hamers, Ann. Rev. Phys. Chem. **40**, 531 (1989).
- ⁴⁹The electron spectroscopic data pertain mostly to *d* electrons. Similar effects, however, are expected for *s*- and *p*-like electrons.
- ⁵⁰Hamamatsu Inc., photomultiplier type R268.

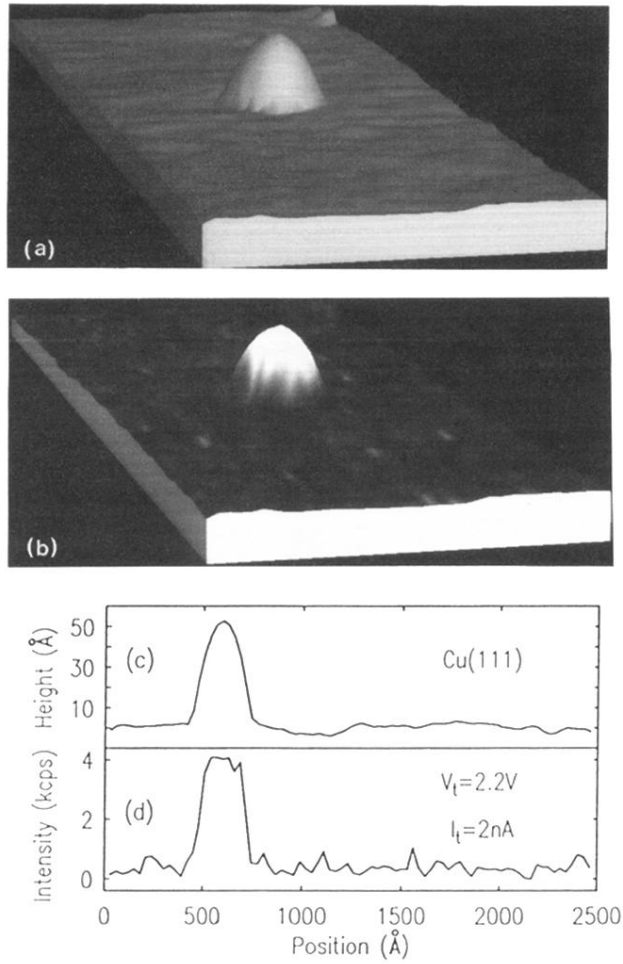


FIG. 1. $1600 \times 2000\text{-}\text{\AA}^2$ subarea of a topograph of a Cu(111) surface ($V_t = 2.2\text{ V}$ and $I_t = 2\text{ nA}$) (a) Topograph (height scale: 50 \AA) rendered as a pseudo-three-dimensional object. (b) Image (a) with photon intensity data superimposed as a grey scale coloration corresponding to 0–2000 cps. (c) and (d) Cross sections of original topograph and photon map, respectively.

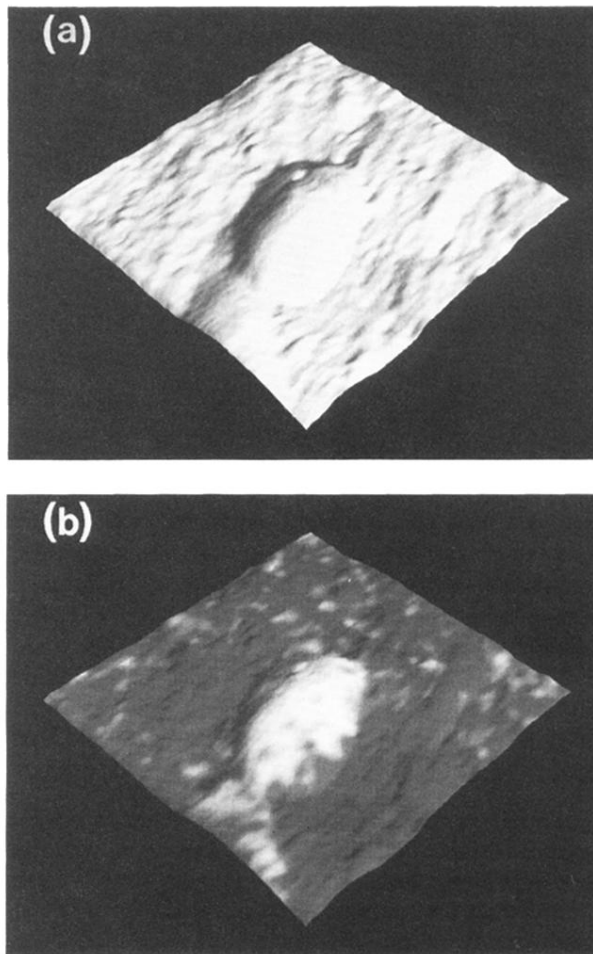


FIG. 2. Topography (edge enhanced) (a) and photon intensity map (b) of a $\sim 300\text{-\AA}$ -thick Ag film on Si(111) annealed at 490 K. Scan area: $350 \times 350 \text{ \AA}^2$, $V_t = -3.4 \text{ V}$, $I_t = 1.5 \text{ nA}$; height scale: 50 \AA ; photon intensity scale: 3000 cps.

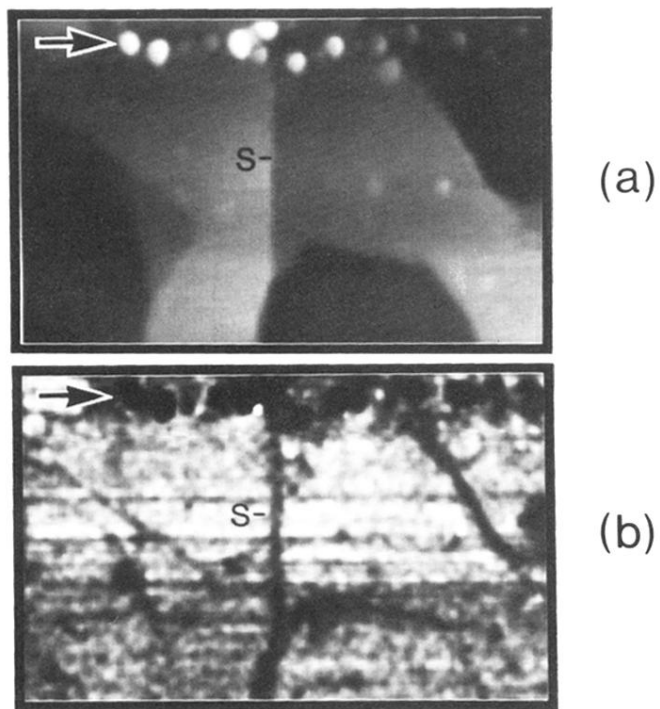


FIG. 3. (a) Constant current topography and (b) photon STM images of a Cu(111) surface exhibiting terraces separated by steps (see marker *S*, for instance) and small structures indicated by arrows which were created by a series of electric-field pulses at positive tip polarity. $V_t = 2.2$ V, $I_t = 5$ nA. Area = 500×300 Å²; intensity scale = 6000 cps. From Ref. 4.

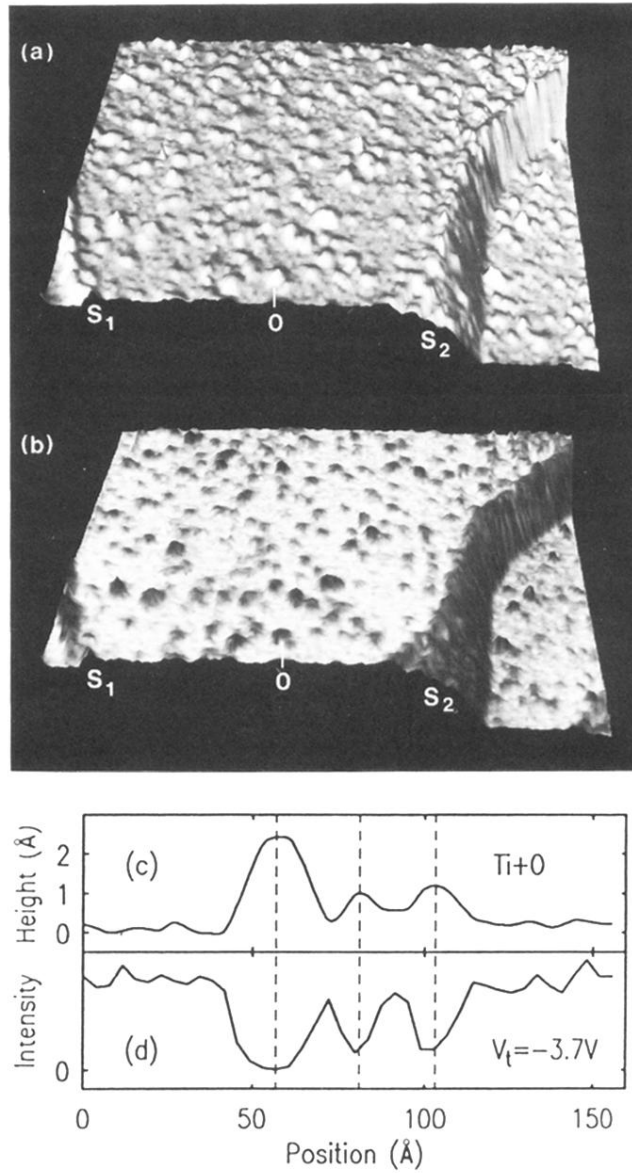


FIG. 5. (a) The STM topograph of a Ti film exposed to 20 L of O_2 at room temperature (area: $1000 \times 1000 \text{ \AA}^2$; height: 20 \AA , $I_t = 50 \text{ nA}$, $V_t = -3.7 \text{ V}$). Examples of steps [S_1 , S_2 and oxygen-induced structures (O)] are marked. (b) A photon map recorded simultaneously (intensity scale: 1000 cps). (c) and (d) Cross sections through an area containing three oxygen-related structures. Dashed lines serve to guide the eye. From Ref. 33.

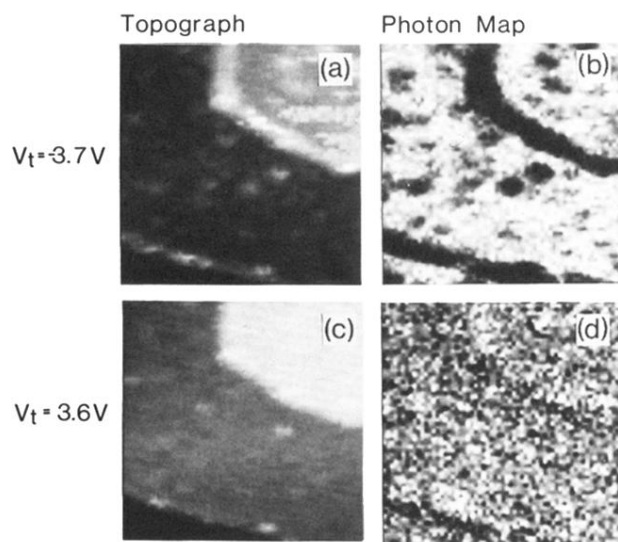


FIG. 6. Bias dependence of STM topographs (a) and (c) and photon maps (b) and (d) of a Ti film exposed to 20 L of molecular oxygen. $I_t = 10\text{ nA}$, $V_t = -3.7$ (top row) and 3.6 V (bottom row); area: $170 \times 170\text{ \AA}^2$; height scale: 7 \AA ; intensity scale: 0–200 cps.

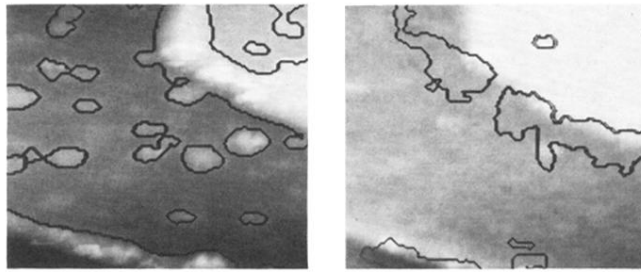


FIG. 8. Topographs of Fig. 6 with contour lines of the corresponding photon maps. Each of the photon maps was averaged before the contour plots were generated. (a) $V_t = -3.7$ V; contour level: 90 cps; and (b) $V_t = 3.6$ V, contour level: 55 cps.